Case History

Laser-scan and gravity joint investigation for subsurface cavity exploration — The Grotta Gigante benchmark

Tommaso Pivetta[1] and Carla Braitenberg[1]

ABSTRACT

We have studied a big karstic cave (Grotta Gigante) in northern Italy using an innovative combination of laser-scan and gravity data. We aimed to forward model the gravity anomaly due to the cavity, verify its compatibility with the Bouguer field, and identify the eventual presence of other sources of gravity anomalies. A sensitivity study was performed preliminarily to assess the minimum size of bodies that could be detected by the gravity surveys. The 3D density model of the Grotta Gigante was constructed using as a geometric constraint the laser-scan data set, which mapped the internal morphologies of the cave, and density measurements on collected rock samples. The laser point cloud was reduced in data density, filtered from the outliers, and subdivided into two surfaces representing the vault and the floor of the cave, to correctly define the prism model. Then, a mean density value,

obtained from laboratory measurements, was assigned to the prisms. We computed the gravity effect of the model in the same points at which the gravity field had been measured. Excellent correlation was found for the cavity; some gravity anomalies were revealed in the surrounding area of the Grotta Gigante that could be effected by other underground karstic morphologies. We attempted to estimate the probable size and depth of the causative bodies, compatible with the geologic environment. This site testified to the goodness of gravity methods for the exploration of such structures, that is, particularly important for risk assessment in a karstic area. The cave itself, the biggest tourist cave worldwide, represents an upper limit for expected gravity signals. The combination of exact knowledge of the causative body and the related gravity anomalies composed a unique data set (that we released to the public, as a benchmark), useful for testing inversion and forward model gravity algorithms.

INTRODUCTION

The Grotta Gigante, according to the 1995 Guinness World Records, has been certified as the biggest tourist cave worldwide. It is located in the northeastern part of Italy, in the Classic Karst plateau (Figure 1) near the city of Trieste, and it is principally composed of a wide ellipsoidal hall of approximately $100 \times 60 \times 70$ m³, two main galleries connecting it to the surface, and southward, a very deep karstic shaft (of approximately 180 m extension). For its isolated position and for its impressive dimensions, the cave is chosen by Marussi (1960) as the ideal site for the horizontal pendulum geodetic station. In addition to this, the Grotta Gigante

holds a seismographic station (Costa et al., 2010) and other geophysical instrumentations for environmental studies (Del Maschio et al., 2011).

The genesis of this cave is related to the karstification process acting on the Aurisina limestones (Cucchi and Piano, 2013) during the past 10 Ma and to different rock collapses that progressively enlarged the structure. In rainy (or warm) periods, the cave was almost completely filled by clayey deposits, which currently cover the basement of the cave.

Since the eighteenth century, the Grotta Gigante cave has been intensively explored to get a better understanding of the complex drainage network and also to evaluate the structural risks connected

---

to the karst environment; several topographic surveys have been carried out over the past 70 years (Marussi, 1953; Busà, 1975), and two long galleries (greater than 50 m) near the surface have been discovered and accessed. Some geophysical surveys were also attempted, but due to the rough topography and to logistic difficulties inside the cave, only potential field methods (gravimetry) and an innovative muon study (Caffau et al., 1997) could be exploited to explore the underground structures. A negative gravity signal of approximately 1.5×10^{-5} m/s^2 amplitude spread over a region of 300×200 m^2 above the cave has been detected (Zanolla et al., 1996); however, only partial modeling studies on the signal have been conducted in the past few years.

In recent years, increased interest in using geophysical methods for subsurface exploration and delineation of karstic structures is testified by numerous publications (Kaufmann, 2014; Martinez-Moreno et al., 2014), and the Grotta Gigante is an ideal site for applying and testing such methodologies.

Still, nowadays some uncertainties about the evolution in time of the cave and its complete extension remain. We currently do not know how deep the sediment infilling is or if there are some other karstic hypogeal morphologies linked to the cave.

In light of the geologic hazard evaluation connected to the karst environment and for a better characterization of the site, particularly important also for the scientific studies conducted inside the cave, we propose an investigation of the Grotta Gigante and the surrounding structures by a forward modeling approach of the gravity field.

We use new laser-scan data acquired inside the cave and density measurements on rock samples to construct a 3D density model of the Grotta Gigante by means of prism representation (Nagy et al., 2000). Then, the modeled gravity field is computed and compared with the recent superficial gravity observations carried out in the surroundings of the cave.

The workflow of the modeling study is as follows. We start presenting the methodology used and the data available to construct our physical model; then, a sensitivity analysis on synthetic examples of Karst morphologies, useful to assess the signal amplitude of various sources of gravity signals, is discussed. Subsequently, elaborations on the laser-scan point cloud to obtain the 3D prisms representation and the density measurements are presented. A final comparison of the modeled and observed gravity fields and conclusions constitute the last sections.

The combination of prisms and gravity observations is a unique data set representing a natural cave, which is a benchmark for testing inverse and forward modeling algorithms. The cave is one of the biggest caves worldwide, and therefore, it acts as an upper limit for a gravity signal that can be expected for a natural cave.

METHODOLOGY AND DATA PRESENTATION

Our study aims to quantify the gravity effect of the Grotta Gigante cave through a forward modeling approach and verify its compatibility with Bouguer data. The gravity observation database consists of two surveys: the first one, realized in the 1970s by the Osservatorio Geofisico Sperimentale (OGS) (Zanolla et al., 1996), is composed of 200 microgravimetry measurements covering an area of 1000×1000 m^2 around the cave. The data set at our disposal does not include the free air observations, only the Bouguer field is reported; details on the acquisition and correction methodology could be found in Zanolla et al. (1996).

The second survey, acquired in 2013 by the University of Trieste, the Politecnico di Milano, and the OGS, gathers 75 new gravity stations in a less widespread area with respect to the previous campaign. These gravity measurements have not been linked to the geodetic network; hence, we only deal with relative gravity values.

This data set needs to be corrected for the topographic effect, so we calculate this correction using prism discretization of different digital elevation models available with decreasing resolution with distance.

For the area immediately above the cave (450×450 m^2), we rely on an airborne laser-scanning (ALS) survey that presents a point cloud representation of the topography with more than 15 million points and a datum density of 15 points/m^2 (Paganini and Pavan, 2012). For our topographic correction, the data are regridded to a resolution of 1×1 m^2 by arithmetic averaging.

The Regional Digital Elevation Model (Regione Autonoma Friuli Venezia Giulia, 2006), with resolution of 10 m, is used for an external area of approximately 9 km^2 surrounding the ALS survey. The cave is only a few kilometers from the Slovenian border, which limits the use of the regional DTM. We, therefore, integrate the SRTM database (Regione Autonoma Friuli Venezia Giulia, 2010) for the reconstruction of onshore topography, whereas for the sea bathymetry, the EMODnet model (European Marine and
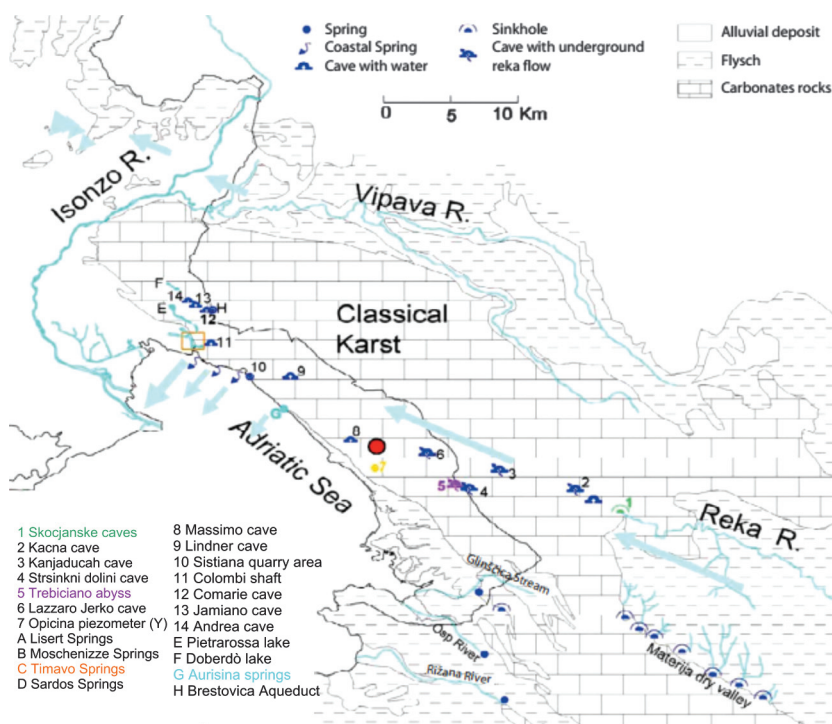

Figure 1. A simplified geologic map of the Classic Karst. The main caves and springs are reported. The red circle locates the Grotta Gigante cave (after Cucchi et al., 2001).

Legend:
- Spring
- Coastal Spring
- Cave with water
- Sinkhole
- Cave with underground reka flow
- Alluvial deposit
- Flysch
- Carbonates rocks

0 5 10 Km

1 Skocjanske caves
2 Kacna cave
3 Kanjaducah cave
4 Strsinkni dolini cave
5 Trebiciano abyss
6 Lazzaro Jerko cave
7 Opicina piezometer (Y)
A Lisert Springs
B Moschenizze Springs
C Timavo Springs
D Sardos Springs
8 Massimo cave
9 Lindner cave
10 Sistiana quarry area
11 Colombi shaft
12 Comarie cave
13 Jamiano cave
14 Andrea cave
E Pietrarossa lake
F Doberdò lake
G Aurisina springs
H Brestovica Aqueduct

Observation Data Network, 2006) is used. Both of these models are resampled to a resolution of 200 m and are covering an area of approximately 1° radius around the Grotta Gigante. The topographic grids are converted into a Cartesian coordinate system (UTM33/WGS84), and the quotas are converted to ellipsoidal heights. The DEM quotas, provided in orthometric heights, are corrected for the geoidic undulation. The gravity effects of all these topographies are computed on each point of the gravity survey and then subtracted from the free-air anomalies. The topographic effect in the area immediately above the Grotta Gigante ranges from 34.3 to 35.2×10^{-5} m/s^2.

The Bouguer fields of these two gravity surveys show that the cave is associated with a negative gravity anomaly of 1.5×10^{-5} m/s^2 amplitude extending more than 250 m. As already mentioned above, no gravity forward or inverse modeling on the new detailed gravity field above the cave has been carried up until now, the goal of the present work.

The geometric constraint for our 3D density prism model is derived from a recent laser-scan campaign, planned in 2011 to map the inner karstic morphologies in great detail and create a virtual tour of the cave.

In this survey, Fingolo et al. (2011) initially define a system of more than 70 benchmarks inside the cave, using classic topographic techniques. Subsequently, based on this internal reference network, they acquire the whole laser-scan data set, that consists of 4.5 billion points. The successive elaboration steps allowed for reduction of the spatial density of data and to georeference the point cloud. The final result is presented in a digital file (size >3 Gb) that contains more than 150 million points in UTM33N/WGS84 coordinates, with a mean datum density of 10,000 points/m^2 and an accuracy of 5 mm at a distance of 150 m. The point clouds must be treated to obtain the internal surfaces of the cave and remove the outliers due to artifacts in the laser-scan acquisition. The laser-scan data allowed us to successfully map the entrance, the actual tourist exit tunnel, and the principal hall of the cave; no topographic data are available for the superficial galleries and for the karstic shaft.

Relying on this internal laser-scan acquisition, we aim to discretize the Grotta Gigante into prismatic rectangular cells and extract two quota values from the laser-scan point cloud, representing the top and bottom of the cave for each cell. Every prism is, therefore, geometrically defined by coordinates x_1, x_2, y_1, and y_2 (Figure 2) of the base cell and the two quota values that limit the vertical extension.

The density constraint is obtained by measuring the bulk density from 20 rock samples collected inside and outside the cave. The samples consist in a series of limestone rocks of various dimensions ($10^{-5} \div 5 \times 10^{-4}$ m^3) divided into two different sedimentary facies ("dark" and "light" limestones) both belonging to the Aurisina Limestone Formation (Cucchi and Piano, 2013). Also, three cores of the clayey sediments were extracted, using hollow punches, from the cavity floor. The density value is determined through hydrostatic weighing principle using a precision balance. For the incoherent sediments, we impermeabilize the samples using paraffin wax.

SYNTHETIC SIGNALS OF SIMPLIFIED KARSTIC MORPHOLOGIES

As we already hinted at, the laser-scan survey does not include topographic data of the karstic shaft and of the shallower galleries; also, the vertical extension of the sediment infilling is still an open

question. Estimating the gravity effect of these structures by the production of simple and realistic synthetic models allows us to check the effective contribution of these sources to the cave observed signal and also to assess the level of approximation of our final model presented in the following sections.

In the following, some simplified density models (Figure 3b and 3c) and their corresponding signals of the Grotta Gigante cave and other karstic structures (Figures 3a and 4) are shown. The vertical section of the model is shown in Figure 3b, the projection of the cave to the surface is given in Figure 3c. Constraints on shape and density contrasts of the causative bodies are derived from literature data (Carulli and Onofri, 1969; USGS, 2006). We compute the gravity effects of the cave, the sediment infilling along profile AC of Figure 3c, and of the karstic shaft on profile AB of Figure 3c. The profiles roughly follow the main direction of the cave. We simulate the measurements on the topographic surface (filled triangles in Figure 3b) and inside the cave (empty triangles) as is observed in the sketch given in Figure 3b.

In Figure 3a, the black dashed and solid lines represent the signal generated by the cave's geometry, which we can reveal by the laser-scan survey (white prisms in Figure 3b), so it represents an estimation of the signal that we would expect after the elaborations presented in the following sections. The cave is associated with a gravity minimum of greater than 1.5×10^{-5} m/s^2 amplitude on the surface, which extends over an area of approximately 200×300 m^2; in correspondence of the entrance a local minimum with amplitude of 0.5×10^{-5} m/s^2 is also evident. We note that gravity and microgravity observations carried out in past years are sufficiently precise (error $\pm 0.01 \times 10^{-5}$ m/s^2; Torge, 2001) and widespread to completely detect and reveal the gravity anomaly. The solid line corresponds, instead, to the gravity effect of the cave as sensed by internal measurements. The wavy pattern is
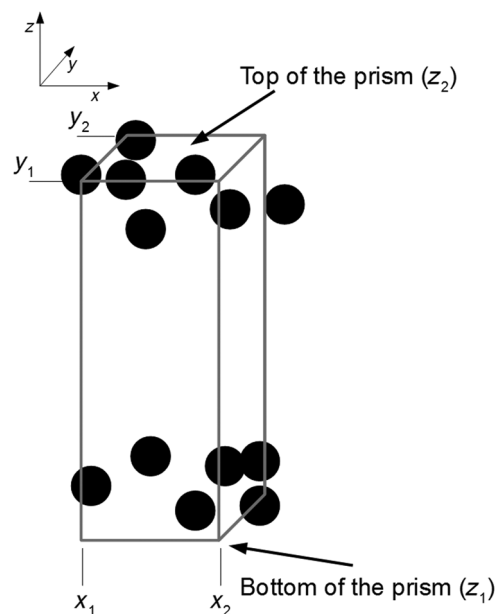

Figure 2. Sketch illustrating the conversion of a point cloud to a prism representation. Each prism is defined by four coordinates (x_1, x_2, y_1, y_2), limiting its areal extension, top (z_2) and bottom (z_1), which define the vertical extension and a density value.

due to the inner topography and the changing height of the stations. In addition, the stations are closer to the anomalous source with respect to the surface stations.

The second series of models includes an estimation of the sediment infill effect. The clayey deposits have been modeled with prisms that reproduce a basin shape (depth of 70 m, area of
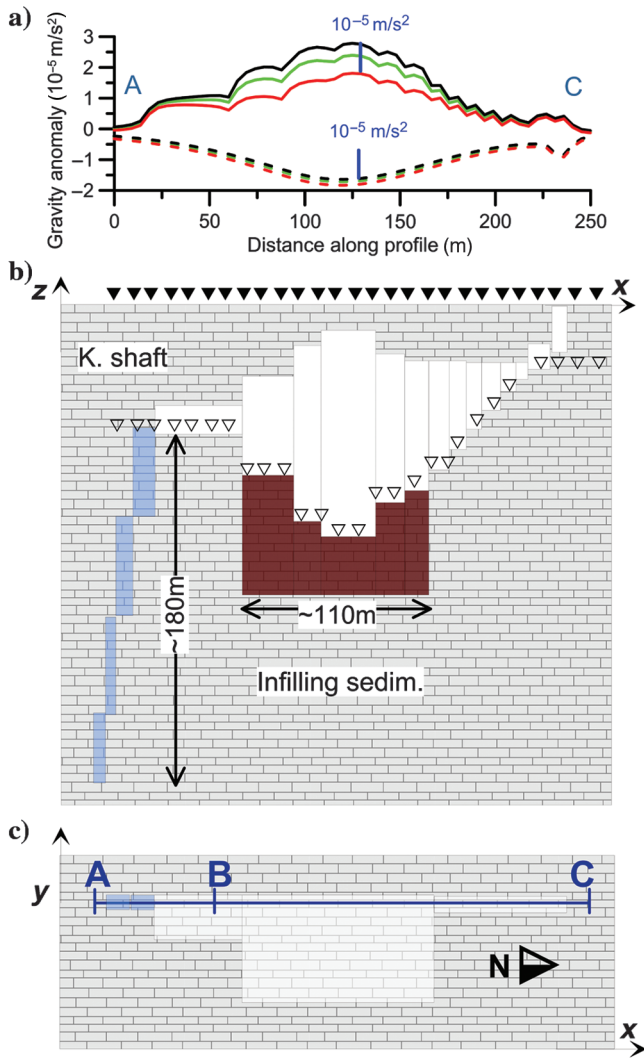

Figure 3. Model geometry (b and c) and related gravity anomalies (a) of the cave and sediment infilling. (a) Gravity effect of the cave (black lines) and of the cave + sediment infilling computed on section A-C: dotted lines are superficial measurements, whereas the solid lines represent the simulated internal measurements. Two different density contrasts clay/limestone are tested: -400 kg/m^3 (green line) and -900 kg/m^3 (red line). (b) Vertical section representing various geologic structures whose gravity signal was simulated: We use prism representation to reproduce the cave, the basin containing infilling sediments, and the karstic shaft that deepens in the southern part of the cave. Filled triangles locate the superficial gravity measurements, whereas empty triangles show the simulated gravity station inside the cave. (c) Plan view of the model; the profiles traced are represented with blue lines. The cave volume is projected as white areas to the surface, and the cave shaft as shown as blue areas. Profiles AB and AC are used in Figures 3a and 4, respectively.

$60 \times 110 \text{ m}^2$, and two different density contrasts of -1000 and -400 kg/m^3).

The dashed lines in Figure 3a represent the superficial gravity anomalies of these models: The green and red lines correspond to the cumulative effect of the cave and the basin with varying infilling densities, whereas the black line is the signal of the only cave model mentioned above. Conversely, the colored solid lines show the gravity effects of the same models computed on the profile inside the cave.

The sediment infilling causes a negative gravity signal at the surface that emphasizes the cave's minimum; however, in this case, the amplitude of the anomalies for the three models is not so different, with deviations of approximately $0.05 - 0.15 \times 10^{-5} \text{ m/s}^2$. Instead, measurements simulated inside the cave show a positive signal with marked differences between the three models. The presence of the infilling sediments has a damping effect on the gravity anomalies; depending on the density contrast between limestones and clays, we have deviations in the gravity anomalies ranging from 0.5 to $1 \times 10^{-5} \text{ m/s}^2$. In both cases (inside and outside the cave measurements), the wavelength of the signal is approximately 200 m.

The effect of the karstic shaft is estimated with four prisms that deepen in the southern part of the cave (Figure 4). As in the previous models, the dotted lines represent measurements on the surface, whereas the solid lines are measurements conducted inside the cave. In both cases, the signal is a gravity minimum. With respect to the sediment-infilling models, the shaft effect is much poorer on the surface, whereas inside the cave, due to a greater proximity to the source, the signal minimum is amplified. In this last case, the signal has an amplitude of $0.2 \times 10^{-5} \text{ m/s}^2$ and a wavelength of approximately 5 m.

The last series of synthetic models, presented in Figure 5, estimates the surface gravity effect of the greatest calcareous stalagmite (Colonna Ruggero) in the cave, and of a gallery 60 m long (Galleria del Fango) situated near the actual tourist exit. The column has been discretized by a vertical prism with base of $1.5 \times 1.5 \text{ m}^2$, height of 12 m, and base located at 50 m depth. The associated signal is a very small positive gravity anomaly (less than $1 \times 10^{-8} \text{ m/s}^2$), which extends more than 100 m on the surface.

The gallery is a horizontal prism extending for 60 m with a section area of 4 m^2 posed at a -10 m quota from the surface.
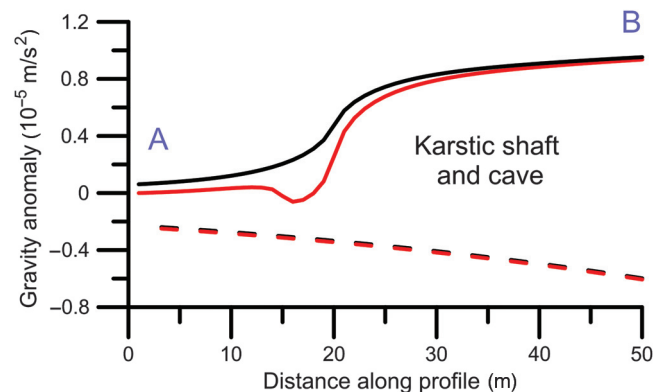

Figure 4. Gravity effects of the cave (black line) and the cumulative effect of the cave and karstic shaft (red) along the profile AB of Figure 3c. As in previous figures dotted lines are superficial measurements, whereas solid lines are measurements conducted inside the cavity.

For this model, we find a gravity minimum characterized by 0.02×10^{-5} m/s^2 in amplitude and wavelength of 100 m.

From the models presented in this section, we note that all of the karstic structures and morphologies are simulated to produce scarce superficial gravity effects compared with the cave's signal (one or more orders of magnitude smaller). The sediment infilling seems to give the greatest gravity contribution: On the topographic surface, it amplifies the minimum associated to the cave by 12% in the case of a density contrast of -1000 kg/m^3, whereas it is by 4% in the other case (density contrast -400 kg/m^3). The superficial gallery, located near the tourist exit path, and the karstic shaft create small gravity minima on the surface, with an amplitude of less than 0.02×10^{-5} m/s^2 and wavelengths of approximately 100 m. The gravity data sets acquired up to now could hardly resolve these signals: Such structures require accurate microgravity measurements with high-spatial resolution (<20 m) to be correctly detected and interpreted.

From simulated measurements inside the cavity, we gain some interesting indications for future gravity campaigns. In fact, the infilling sediments and possible karstic conduits developing under the cave basement could be investigated and characterized by measuring the gravity field inside the cave, where the signals are amplified with respect to the surface by more than 10 times.

ELABORATION OF THE LASER-SCAN POINT CLOUD: GEOMETRIC CONSTRAINT OF THE MODEL

As previously outlined, we rely on the laser-scan internal acquisition for the construction of our 3D density model of the cavity. The impressive characteristics of the data set in terms of precision and

resolution have led to a topographic representation of the cave with more than 150 million points. Such a data set (3 Gb) needs to be analyzed in sectors and then reduced in spatial resolution to decrease the computational effort, also paying attention to keep the main morphological features. Moreover, the data set points are not divided between the surfaces constituting the roof and the floor of the cave. Therefore, to correctly define the vertical extension of each prism, we have to find a method for separating the points between the two interfaces and then extract the quota information. In addition to this, we also need to filter out some outliers present in the original data set. As evident, elaborating such a big data set, using a common PC, requires the development of efficient and automatic computer procedures.

In the following paragraphs, we present all the processing steps and algorithms necessary to automatically manage the transition from the original point-cloud data to the prisms representation.

Averaging on cells

The first algorithm uses an averaging process acting on square cells to reduce the spatial resolution of the data set and obtain a first separation of the points between the top and the bottom of the cave.

Figure 6 exemplifies the functioning of such a technique: In practice, the program subdivides the cave's area into cells of 0.5×0.5 m^2 and calculates for each cell the mean quota. The points belonging to the roof surface (top) are defined as those above the mean quota (cyan circle), whereas those of the floor (bottom) are defined as the points below the mean quota. Finally, the points of the two interfaces are averaged separately to obtain a reduction of the data density. An application of this method on a sector of the Grotta Gigante cave is shown in Figure 7, where the green circles represent the original data, and the black squares and the red triangles constitute, respectively, the floor and the roof of the cavity after the elaborations. We note from the Figure 7 that the cave's morphologies are smoothed by the averaging process; however, the main topographic trends are well maintained. This is also testified by the standard deviation computed for each cell of top and bottom, that in absolute value is less than 0.5 m.
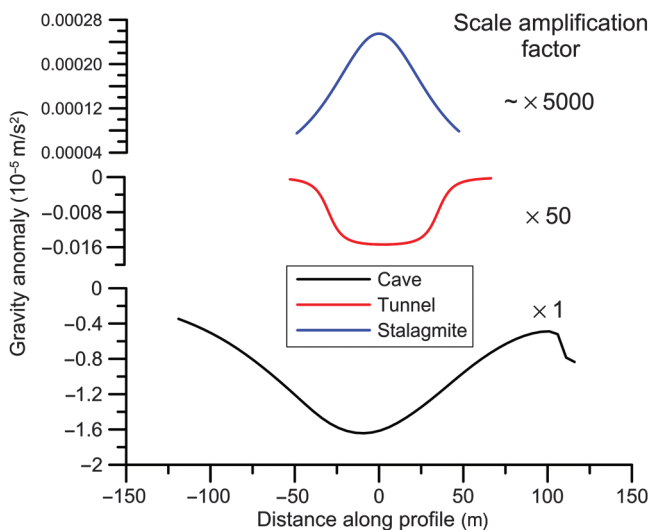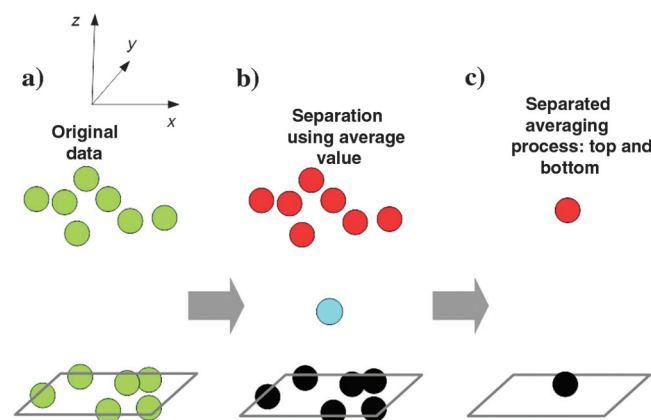

Figure 5. Gravity effects calculated at the surface of the stalagmite Colonna Ruggero (blue line) and of a superficial tunnel (red line) compared with the cave's signal (black line). Colonna Ruggero is composed of a prism ($1.5 \times 1.5 \times 12$ m^3) with base at -50 m. The tunnel is a horizontal prism ($2 \times 2 \times 60$ m^3) posed at -10 m quota; the gravity profile is traced following the direction of development of the tunnel. Respect to the scale of the gravity of the cave, the scales for the tunnel and the stalagmite are amplified by a factor of 50 and 5000, respectively.

Figure 6. Sketch representing the first algorithm for decimation and separation. (a) A cell (0.5×0.5 m^2) of the original laser-scan data, (b) the calculation of the mean quota value and discrimination between two surfaces, and (c) the separate averaging process on both surfaces.

Some critical aspects are present, too: The red ellipse enhances an area in which we have found a mixture between the points of the top and the bottom; this situation, that seems to reproduce a calcareous column, is an artifact caused by the inhomogeneous spatial distribution of the laser-scan data set. The sketch proposed in the Figure 8 helps us to better understand the origin of this phenomenon: An obstacle present in the cave creates a shadow zone, where laser points from the ground are absent and only the roof morphology is reconstructed. As a consequence, the averaging process (acting on cells) calculates a mean quota that is inside the point cloud constituting the vault, and so, the discrimination between the top and bottom does not work correctly. The cyan ellipse evidences another critical aspect: The averaging process does not remove the outliers ranging outside the cave's area, and so we observe the production of some unreal structures. The subsequent sections present the methodologies used in order, respectively, to eliminate the outliers and improve the separation process.

From this analysis, we also find some areas where vertical superposition of different tunnels is present; this is the case of the tourist exit gallery that superposes the main hall. For such a situation, we extract the points belonging to this branch from the cave's cloud and process them separately.

We have to remark, however, that this first algorithm has allowed a successful reduction of the data point density, an important objective that reduces the computation effort required in the following procedure steps.

Second-order surface fitting

A 3D closed surface that locally approximates the cavity could be a useful tool to eliminate the outliers. As noticed by some authors (Cucchi and Marinetti, 2000), the Grotta Gigante cave has a roughly ellipsoidal shape in some sectors, which suggests fitting a point cloud with a second-order surface. The nine coefficients defining the second-order surface are determined with a best-fit algorithm (Turner et al., 1999). Once the surface has been calculated, the aver-

age distances μ and standard deviations σ between this reference surface and the points of the input cloud are found. The outliers are defined as those values whose distance is greater than $\mu + 2\sigma$, and they are deleted. The procedure is iterated a few times. Before the application of this method, the whole data set, reduced in spatial resolution, is divided into sectors. The dimension of each sector, that is, approximately 30 m, is chosen to eliminate sudden changes in the morphological trends and so to make the local ellipsoidal fitting reasonable.

In Figure 9a and 9b, we show an application of the method to the southern sector of the cave. The laser-scan acquisition in this zone was complicated by logistic difficulties, and therefore, it resulted in a relatively noisy data set, including laser-scan points that seem to be multiple repetitions of the original surface. The fitting algorithm was iterated eight times. In the figure, the best fitting ellipsoid surface is reported together with the outliers filtered out (green circles) and the kept points, which define the cave's morphology (black circles). As is evident, the ellipsoid reached a good approximation of the cave structure, and so the procedure optimally has removed all the outliers present. The procedure has been extended to all the cave sectors (another sector is reported in Figure 9c), including the exit gallery, leading to a complete cleaning of the data set from various outliers.

Local regression and prism definition

The last computation step serves to define the final discretization of the cave in prisms. Finding a surface able to efficiently discriminate the cave's top and bottom seems to be very similar to the problem of determining the best fit surface of noisy data. In fact, we can imagine the points of our relief as noise deviating from the smooth morphological trend of the cave's median plane. For our scope, we are looking for fitting algorithms that create surfaces sufficiently complex to follow the structural undulations of the cave, but at the same time they should be insensible to local gaps in the data set. Figure 10 illustrates this situation along a vertical section
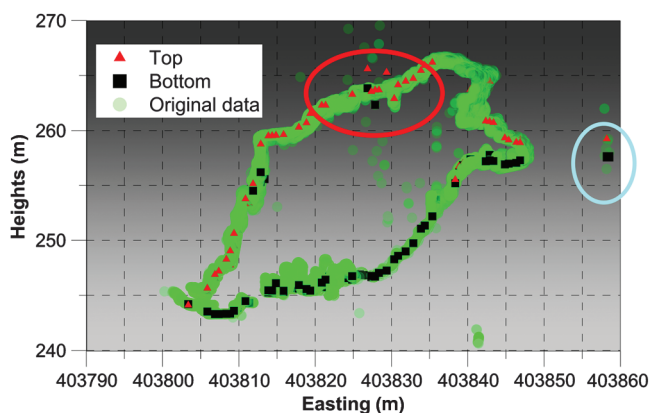

Figure 7. Application of the first algorithm to a sector of the cave. The green points signify the original data. Outliers can be distant from the inner cave surface (e.g., green dots at easting 403,842 m and height 242 m). The black squares signify the decimated bottom, and the red triangles show the decimated top. The red ellipse enhances an area with a mixture of top and bottom interfaces. The cyan ellipse represents some points outside the cave area, probably outliers, that have to be removed.
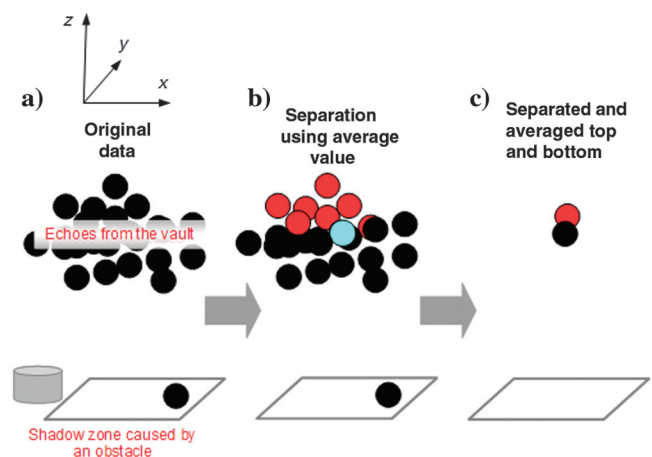

Figure 8. Sketch illustrating the problems arising with the first algorithm: the (a) portion of the original laser-scan data with a marked difference between the number of echoes from the vault and from the basement, (b) application of the averaging process: bad discrimination between top and bottom points due to inhomogeneous distribution of data points, and (c) resulting decimated and separated data set.
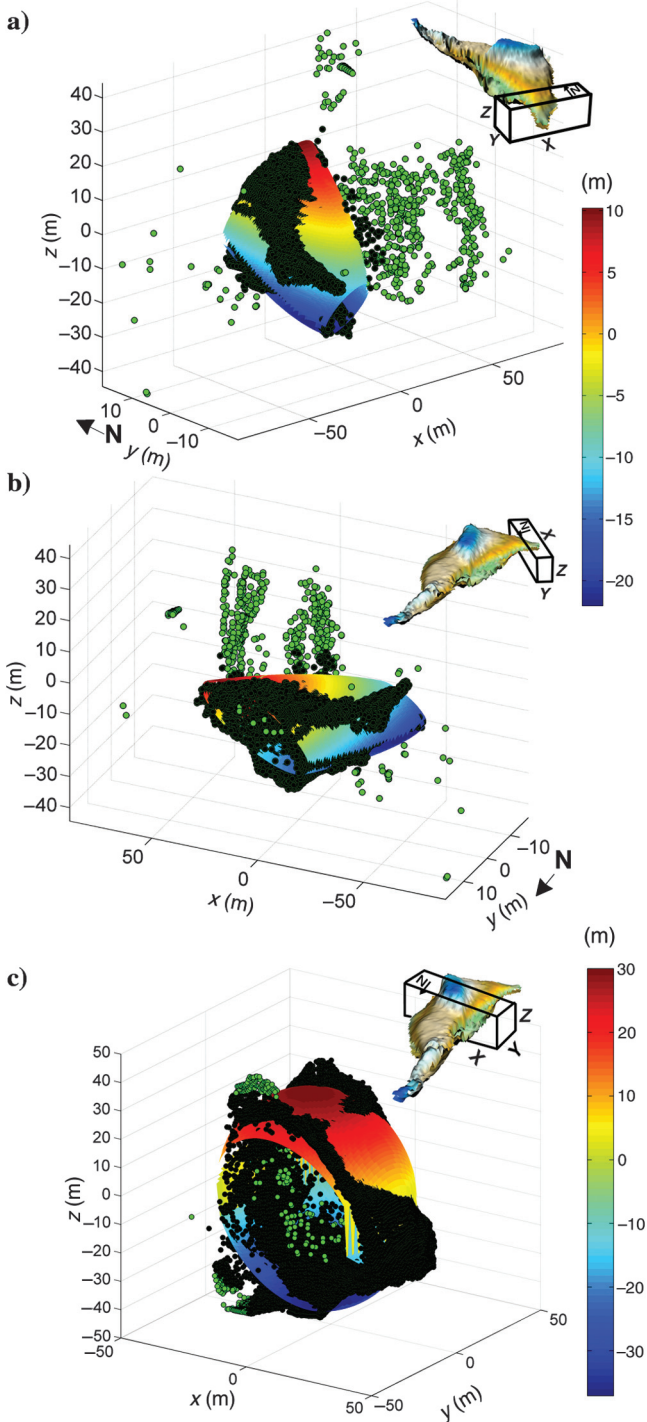
Figure 9. The ellipsoidal fitting applied to two sectors: Panels (a and b) refer to a sector of 30 m width in the southern part of the cave and (c) is a sector located in the central part of the cave. The position of the sector with respect to the cave and the point of view are given in the top-right corner of panels (a-c). The green circles are outliers eliminated by the algorithm, whereas the black circles represent the points kept. The colored surface is the fitted second-order surface, and the color gives the height. The origin of the coordinate system is in the center of the cave's sector.

of the cave. It is seen that a linear plane is not adequate to represent the median surface of the cave, and a higher order surface is needed. The higher order surface allows us to efficiently separate the data points of the bottom from those of the top of the cave (Figure 10b).

The local regression technique (loess; Cleveland et al., 1992) offers the following characteristics: in this method at each point in the data set, a polynomial surface is fitted to a subset of the data using a weighted least-squares method, where the weights decrease with distance. The number of data points (N_{par}) involved in the regression procedure is governed by the parameter α ($0 < \alpha < = 1$), known as a smoothing parameter, which could be interpreted as the percentage of the data points included in the regression process ($N_{par} = N\alpha$, where N is the total number of points). In practice, for each point only the nearest N_{par} points contribute to the estimate of the loess function, so a large α value (i.e., 0.7) creates smooth surfaces interpolating the data, whereas low α values (i.e., 0.003) tend to make surfaces more conformed to the data oscillations.

Often, α is assumed to be 0.25–0.5, for most loess applications (Cleveland et al., 1992). In our case, after some tests, we fix 0.3 as the best value for the smoothing parameter. The total number of points involved in our regression process is approximately 80,000, implying that, assuming $\alpha = 0.3$, more than 25,000 points contribute to the definition of each point of the surface. Once the point clouds (already reduced in spatial density and filtered from the outliers) have been fitted with the local regression surface, we proceed to the definitive subdivision of the points between the two interfaces, as observable in Figure 11. As already stated in the previous paragraphs, the exit gallery has been processed separately from the main hall and the entrance tunnel.

With the top and bottom surfaces reduced in spatial density and filtered from the outliers, the prism model is easily defined (Figure 12). We have obtained more than 40,000 prisms with resolution of 1×1 m^2, which have reproduced the underground structure of the Grotta Gigante cave.

BULK DENSITY MEASUREMENTS: THE PHYSICAL CONSTRAINT

With such a detailed geometric model of the cave, using improper density values for the surrounding rocks could introduce errors in the calculation of the gravity quantities of interest, and therefore,
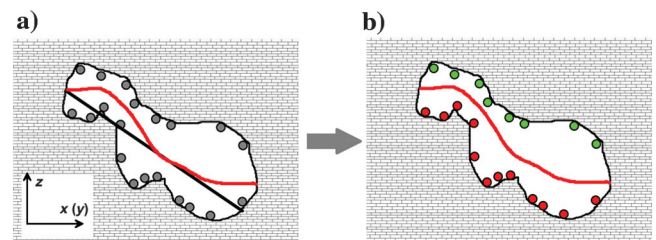

Figure 10. The separation process of laser-scan data shown on a vertical section to obtain the top and bottom of the cave. (a) Two interpolating surfaces are fitted to the point cloud: a plane (gray line) and a high-order surface (red). Only the high-order surface allows us to follow the local cave's morphology. (b) Algorithm with high-order surface separates the red points (bottom of the cave) from green points (top of the cave).

lead to fallacious interpretation of eventual residuals. Accurate measurement of the limestones and clayey sediments bulk density was executed. More than 20 rock samples of various dimensions
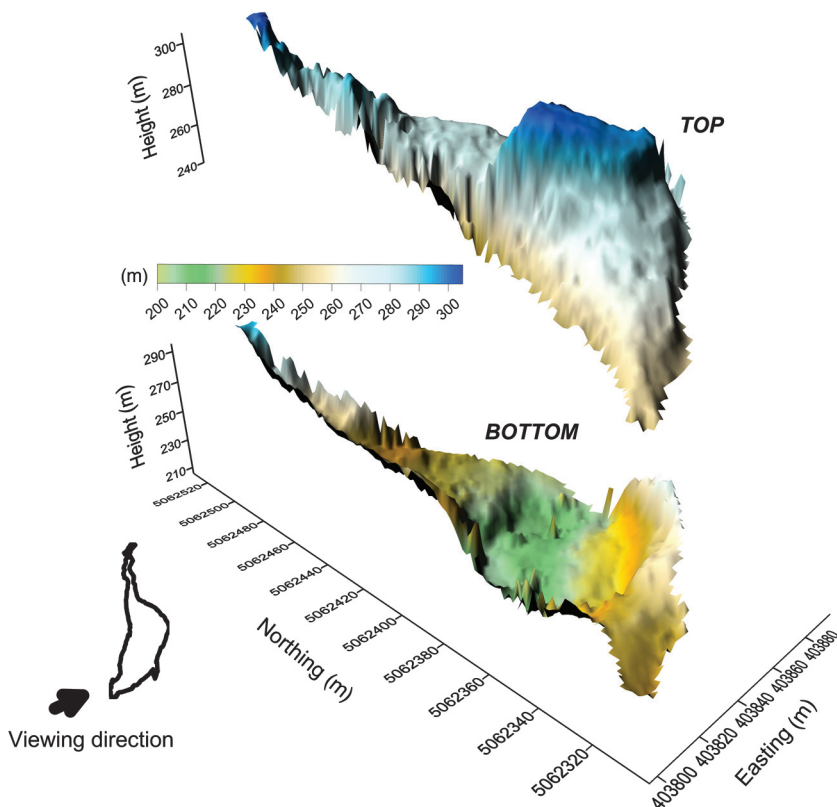
Figure 11. The resulting surfaces of the top and bottom of the entrance and the main hall after the separation process, in which the loess surface has been used. The color scale gives the height.
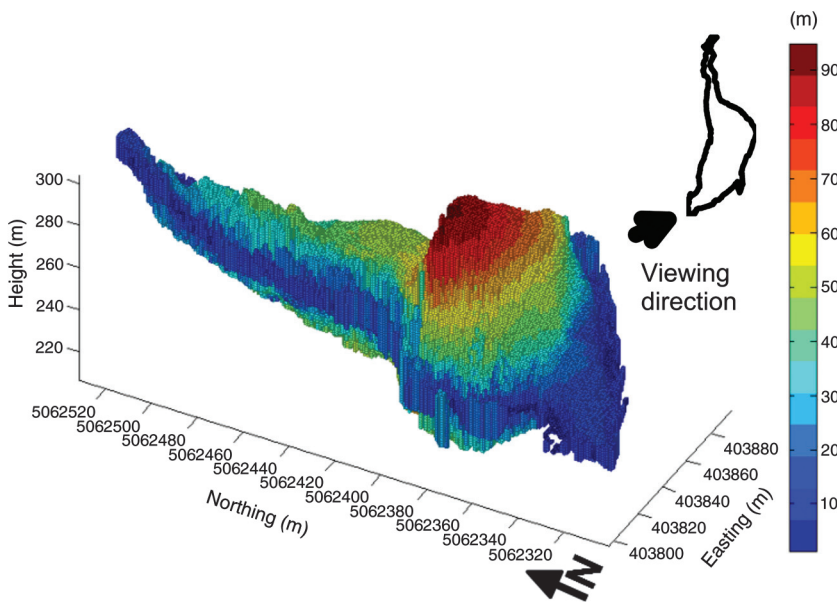

Figure 12. The prism model, as seen form a southern–western perspective, of the entrance gallery and the main hall. The color scale represents the vertical extension of each prism.

were collected inside and outside the cave, and also three cores from the inner deposits were extracted. The rocks have been divided into two sedimentological facies constituting the Aurisina Limestone (Cucchi and Piano, 2013) Formation, which has dark limestones, characterized by the presence of organic matter, and light limestones, which are purer limestones (with respect to the previous) in terms of calcite content.

The bulk density has been determined through the weighting hydrostatic principle. In practice, by measuring the sample's mass in air m_a and suspended in water m_w, we are able to determine the bulk density by the following formula:

$$\rho_{\text{bulk}} = \frac{m_a}{(m_a - m_w)/\ \rho_w}, \qquad (1)$$

where ρ_w is the water density, assumed to be in standard conditions (1000 kg/m^3).

Also, the volume of the submerged body V_b is easily calculable from the difference of the in-air and in-water weights:

$$V_b = \frac{m_a - m_w}{\rho_w}. \qquad (2)$$

For rocks, because they are compact and do not present high porosity and interconnected voids, it was not necessary to impermeabilize the samples, whereas the clayey deposits, contained in iron hollow punches, have been sealed off using paraffin wax. The paraffin's density has been determined by measuring the volume of water displaced by a wax sample and then dividing the mass by it. In Figure 13, the frequency distribution of the various measurements conducted on different paraffin wax samples is reported. We obtain a mean density of 900 kg/m^3 with a standard deviation of ±20 kg/m^3.

Finally, calculating with equation 2, the volumes of the iron hollow punches V_i, of the paraffin wax V_{pf} and of the whole system composed of sediment + hollow punch + wax (V_{pf+i+s}), and obviously knowing the three masses (m_i, m_{pf}, and m_{pf+i+s}) we are able to compute the volume of clays V_s and the bulk density of the clays ρ_s using the following formulas:

$$V_s = V_{pf+i+s} - V_{pf} - V_i, \qquad (3)$$

$$\rho_s = \frac{m_{pf+i+s} - m_{pf} - m_i}{V_s}. \qquad (4)$$

For each sample, at least five measurement repetitions have been preformed to obtain the

statistical error. For the clayey deposits, the paraffin's density uncertainty is also taken into account for the computation of the whole error, using the following formulas derived from the error propagation law:

$$\frac{\partial \rho_s}{\partial m_t} = \left[\frac{m_t}{\rho_t} - \frac{m_{pf}}{\rho_{pf}}\right]^{-1} - \left[\frac{m_t}{\rho_t} - \frac{m_{pf}}{\rho_{pf}}\right]^{-2} \frac{m_t - m_{pf}}{\rho_t}, \quad (5)$$

$$\frac{\partial \rho_s}{\partial m_{pf}} = -\left[\frac{m_t}{\rho_t} - \frac{m_{pf}}{\rho_{pf}}\right]^{-1} + \left[\frac{m_t}{\rho_t} - \frac{m_{pf}}{\rho_{pf}}\right]^{-2} \frac{m_t - m_{pf}}{\rho_{pf}}, \quad (6)$$

$$\frac{\partial \rho_s}{\partial \rho_t} = (m_t - m_{pf}) \left[\frac{m_t}{\rho_t} - \frac{m_{pf}}{\rho_{pf}}\right]^{-2} m_t \rho_t^2, \quad (7)$$

$$\frac{\partial \rho_s}{\partial \rho_{pf}} = -(m_t - m_{pf}) \left[\frac{m_t}{\rho_t} - \frac{m_{pf}}{\rho_{pf}}\right]^{-2} m_{pf} \rho_{pf}^2, \quad (8)$$

where m_t and ρ_t are, respectively, the mass and the density of the system composed by muddy sediments and paraffin, already corrected for the effect of hollow punch masses and densities.

Figure 14 displays the final results: The black circles represent different dark limestones samples, the red circles represent the light ones, and the green circles are some dark limestones with marked superficial alteration (cracks and evidence of chemical aggression). The errors are reported using the common bar representation (1 root-mean-square [rms] error), whereas the label indicates the sample's mass in kilograms. Concerning the dark limestones, we have found a mean density of 2670 ± 10 kg/m³, whereas for light limestones, a value of 2680 ± 20 kg/m³ has been measured. The altered samples have been obviously excluded from the mean density calculus because they have much lower density and must be considered as outliers.

Considering the error estimates, the two types of limestones do not differ significantly in terms of density, so we proceed in calculating an average density representative of both lithologies (2680 ± 20 kg/m³), which is used in gravity field forward modeling.

The clay density measurements are plotted using white circles: Larger differences in the density values with respect to the limestones (1710 kg/m³) and also a greater dispersion in the values are present (± 30 kg/m³). We remark that measurements have been carried out only on three cores, and so they offer a rough approximation of the density value. However, it is evident that limestones and clays produce a marked density contrast that could be of great interest for gravity exploration scopes, as already noticed in the synthetic models.

FORWARD MODELING AND COMPARISON WITH OBSERVED DATA

With the density contrast value between air and limestones and the geometry constraint, the physical model of the underground structures has been defined and we can calculate the gravity signals of interest.

Tesseroids software (Uieda et al., 2010) is used to compute the vertical gravity anomaly of our model in the same points, in which the free-air gravity values have been observed, using formulas from Nagy et al. (2000). To compare modeled and observed fields, we must accomplish some elaborations: First of all, we have to integrate
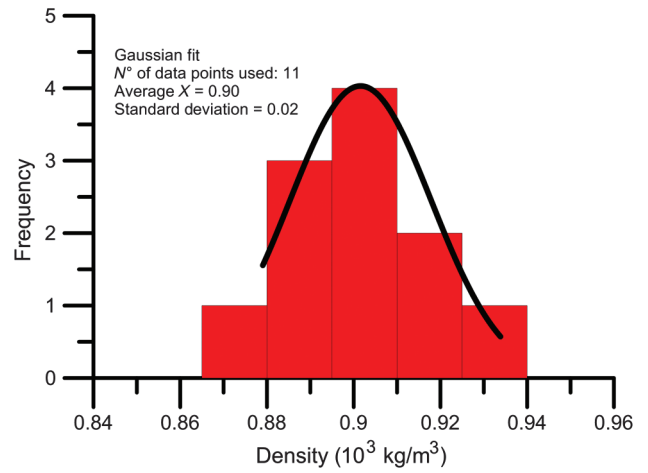

Figure 13. Histogram reporting the frequency distribution of the density values of paraffin wax. A Gaussian curve, fitting the data, is added to the graph with the associated statistics.
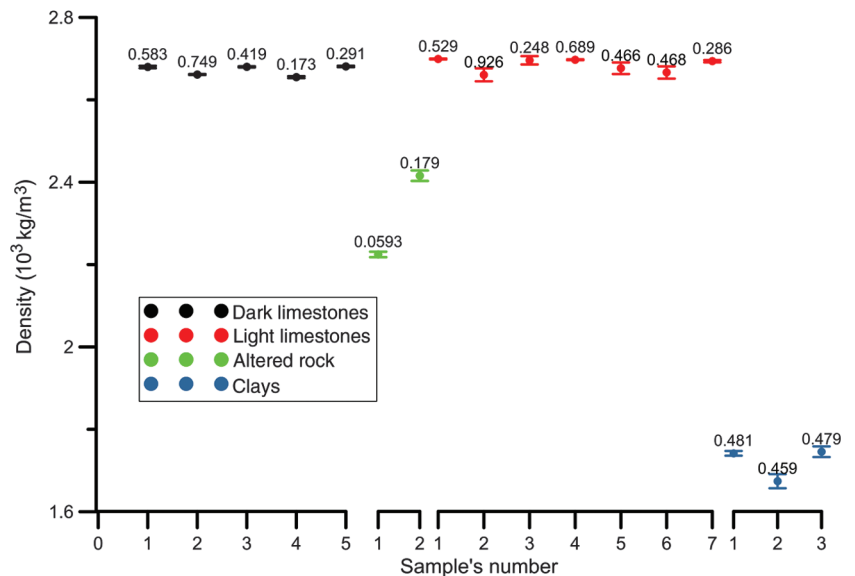

Figure 14. Density measurement results: The black circles are relative to the dark limestone facies, whereas red circles correspond to the densities of the other facies. The green circles are altered rocks, and the white ones represent the sediment cores. For each sample, we performed at least five measurements to get an error estimate, shown as the bar error of $\pm$rms. Labels show the mass of each sample (in kilograms).

the OGS survey ([Zanolla et al., 1996](#)) and the more recent acquisitions. As already hinted at, we only have at our disposal the Bouguer field of the OGS acquisition, so we cannot correct the free-air measurements using our topographic model. In addition to this, the more recent acquisition has not been linked to the geodetic network; therefore, a systematic bias is present in the free-air anomalies. So as to
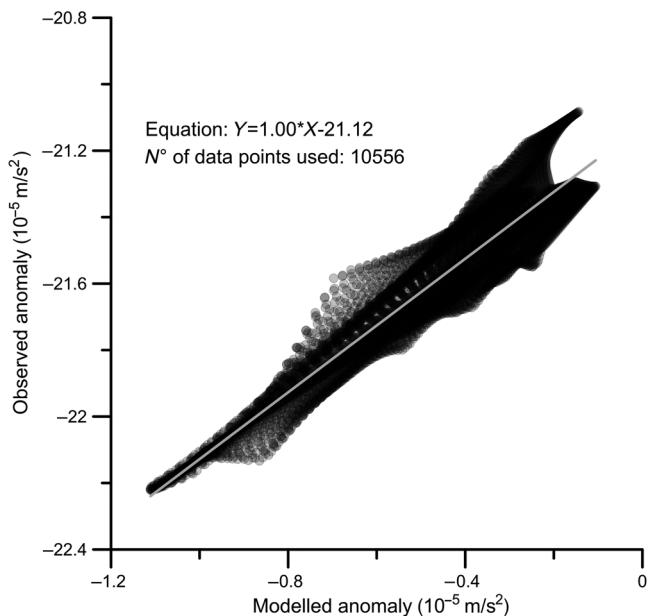
combine the two campaigns, overcoming these two problems, we perform a regression analysis and align the data sets.

Second, another systematic shift exists between the integrated observed data and our modeled gravity field. Similar to the previous case, a regression procedure involving these two grids (Bouguer and modeled field) allows us to estimate the systematic difference (Figure 15) and subtract it from the Bouguer map. Our model includes only the cave and not crustal structure, which obviously creates a bias in the absolute values of the calculated gravity values. For the purpose of this study, the bias is of no interest and can be reduced by the regression analysis.

After such corrections, a comparison between the two fields (observed and modeled) is possible and is presented in the contour maps of Figure 16 and in profiles (Figure 17), where an excellent agreement in terms of amplitude and shape of the anomaly is observable. The largest part of the superficial gravity signal is due to the void of the cavity. The infilling sediments and the karstic shaft, that deepens in the southern part of the cave, produce scarce effects on the surface. Our synthetic models have predicted small but revealable gravity signals for the infilling sediments on superficial measurements also $(0.05 - 0.1 \times 10^{-5} \text{ m/s}^2)$. The absence in the real data of these gravity effects lets us infer that the infill is of smaller size in terms of area and/or maximum depth than the synthetic model.

The residual map (Figure 18a) that corresponds to the difference of observed and modeled data, shows and enhances some unexplained signals. First, we have to note the presence of a regional trend, evident also in the profiles, probably an effect of the noncorrection for the crustal thickness effect and/or to some density inhomogeneities inside the limestones of the karst plateau. However, modeling such structures is not the goal of the present work.

Of more interest is the elongated gravity minimum that develops from the actual tourist entrance toward the north for more than 200 m. Its amplitude is approximately $0.1 \times 10^{-5} \text{ m/s}^2$, and it has a wavelength of 150 m. This signal is not connected to any known underground structure; hence, no constraints on causative bodies are available.

Nevertheless, if we superpose the detailed digital elevation model derived from the laser scan and the residual gravity map (Figure 18b), we appreciate a high correlation between the gravity minimum and the superficial karstic morphologies (sink holes). The broad minimum $(0.15 \times 10^{-5} \text{ m/s}^2$ amplitude; see the black line in Figure 18c) cannot be only caused by the superficial infilling sediments of the sink holes, that usually are composed of clayey deposits and generate harsh density contrasts against the limestones because the wavelength of the observed signal is much wider and covers the entire series of sink holes.

The elongated gravity minimum could be an effect, instead, by local density variations on the Aurisina limestones, maybe due to a more fractured zone, which cause a decrease in bulk density. In the Grotta Gigante area, the presence of tectonic discontinuities (faults) could be expected because caves and sink holes usually

Figure 15. Regression analysis performed on Bouguer observed and modeled values data. Two identical grids of observed Bouguer and modeled field data are plotted and fitted using the regression technique. An excellent agreement is found. The angular coefficient of the line is close to 1, indicating that the amplitudes are quite the same. The bias between the two grid is approximately $21 \times 10^{-5} \text{ m/s}^2$.
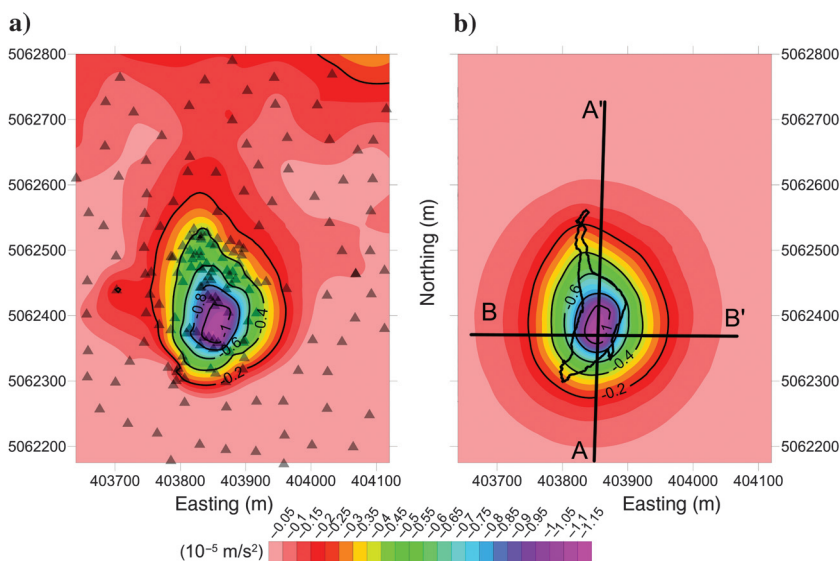

Figure 16. Comparison between modeled and observed gravity fields. (a) Observed Bouguer: The triangles indicate the location of the gravity measurements. (b) Modelled gravity field: The lines trace the profiles presented in Figure 17.
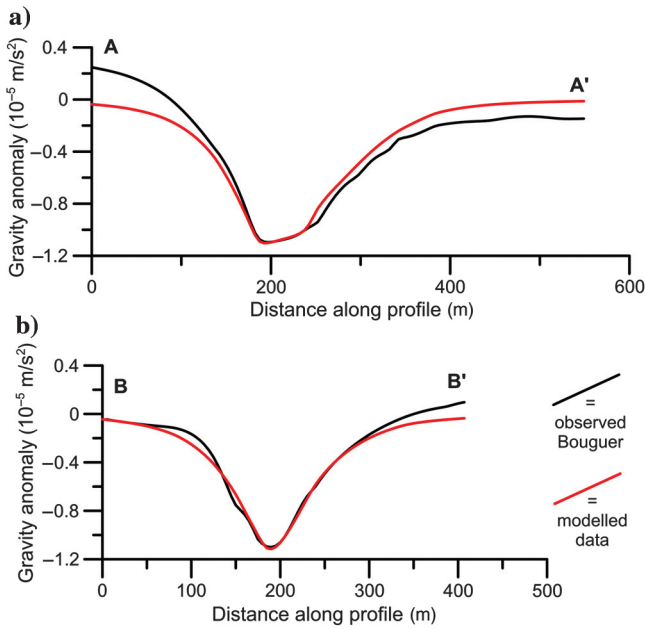
Figure 17. Longitudinal and transverse profiles traced over the gravity minimum of the cave. The red line is the modeled signal, whereas the black line stands for the observed signal. A long wavelength anomaly is tilting the Bouguer in profile AA′, probably due to the noncorrection for the crustal thickness effect or maybe because of some density inhomogeneities in the karstic limestones.

evolve along weakness lineaments. Other possible explanations of the gravity residual minimum involve underground karstic morphologies.

If we hypothesize deeper sources, maybe due to one or more karstic conduits, we can estimate the necessary size. A cylindrical conduit at the depth of 75 m (top) with radius of 10 m could reproduce the signal (dashed blue line in Figure 18c). In Figure 18c, the red line enhances the gravity anomaly due to another model, composed of 50 cylinders of radius 1 m posed at a shallower depth (20 m) with respect to the previous hypothesis.

In synthesis, we find that in the case of a hollow cylinder a depth of 75 m and a radius of 10 m seem adequate. If instead, we had a density reduction due to faulting and karstic conduits, the bulk density contrast would be lower and consequently the volume of the anomalous mass generating the signal must be bigger by a factor that is inversely proportional to the density contrast.

Presently, neither of these gravity anomaly sources can be excluded. The observed and modeled gravity fields (of the more recent survey) and the prism model of the cave are given in the supplementary material, which can be accessed online at s1.pdf, s2.pdf, and s3.pdf.

CONCLUSIONS

In the present work, an innovative integration of laser scan, density measurements, and superficial gravity surveys has been used for studying a karstic limestone cave, the Grotta Gigante. The main aim was to verify the compatibility of the gravity signal derived from a new 3D model of the cave with the observed superficial Bouguer anomalies. We also wanted to check the eventual presence of other sources of gravity signals. First, some synthetic models of the
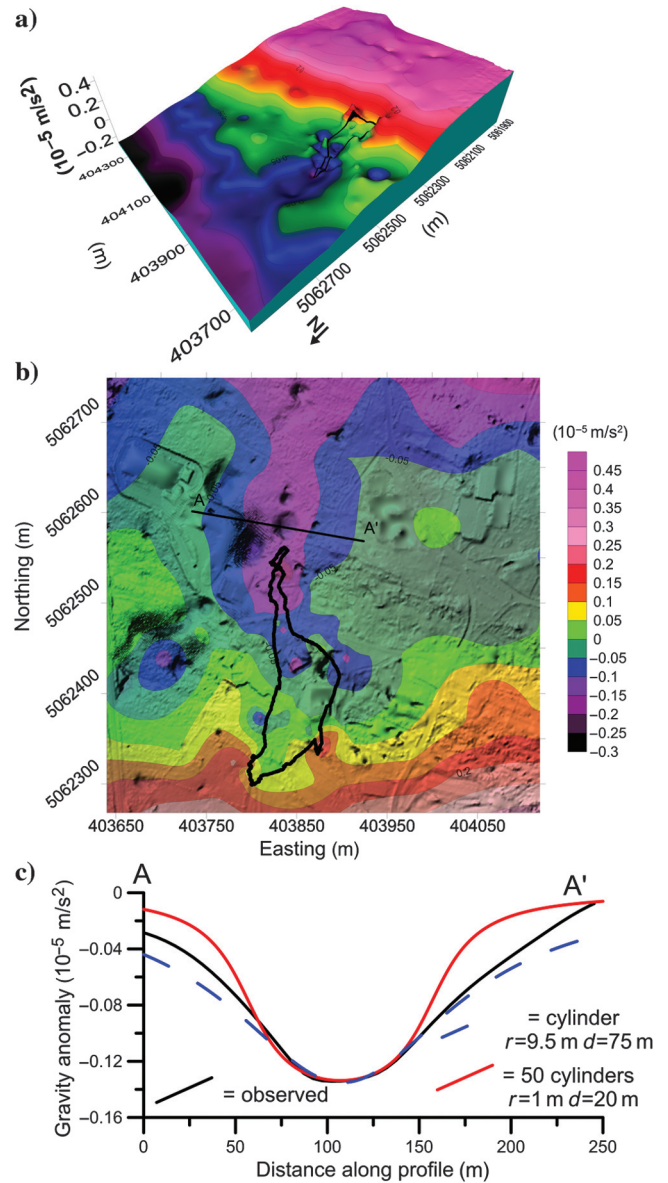

Figure 18. (a) The 3D surface of the residual field, resulting from the subtraction of observed and modeled grids. A long wavelength east–west-striking signal is seen, with northward decreasing gravity values. (b) The topographic map, derived from laser-scan data, superposed on the residual map: A good correspondence between epikarst morphologies and the residual gravity minimum is observable. The cave's outline and the trace of section AA′ are reported. (c) Section AA′ crossing the elongated gravity minimum of the residual map (black line). Dashed-blue line: anomaly due to a cylinder with radius 9.5 m located at 75 m depth. Red line: anomaly caused by 50 adjacent cylinders of 1 m radius posed at 20 m depth.

cave and surrounding structures, as the karstic shaft or the inner infilling sediments, have allowed us to assess and estimate the relative contributions to the gravity anomalies. We have found that the cave should be the principal component on the gravity signals, whereas the karstic shaft and the sediments effects are hardly discriminable with only surface surveys. They could be recovered by internal gravity measurements. Also, the gravity contribution of superficial galleries, not taken into account in our modeling study,

or small morphological structures (such as stalagmites) are clearly insignificant and are also difficult to detect with microgravity studies.

Then, the model of the cavity was constructed using newly acquired laser-scan data as the geometric constraint, and the density values have been determined by direct measurements on rock samples. The elaboration of the laser-scan points has led to the representation of the cavity with more than 40,000 prisms, with base dimensions of $1 \times 1\,\mathrm{m}^2$. The model includes the galleries of entrance, the exit tunnel and the main hall. The densities of limestones have been determined through the hydrostatic weighting method. Two rock facies were sampled, but no bulk density differences between them have been found. Also, a first estimation of the density of the clayey infilling of the cave has been attempted.

The gravity signals have been computed on the same Bouguer observation points. A great concordance was found for what concerns the shape and the amplitude (more than $-1 \times 10^{-5}\,\mathrm{m/s}^2$) of the anomalies. The computation of the residual map has revealed an interesting gravity minimum in the northern part of the tourist entrance, which roughly follows the structural lineament of the cavity. Such a gravity minimum follows the alignment of the numerous sink holes, which develop in the northward direction, continuing the strike axis of the cave. An underground continuation of the cave cannot be excluded. Further investigation of this zone determining the physical characteristics of the clayey sediments of the sink holes and multiparametric geophysical surveys could eventually explain the gravity anomaly.

The effects of the infilling sediments of the big cave have not been revealed on the superficial gravity anomaly maps. Our basin models should be taken as an upper limit for the expected gravity signals; evidently, the real extent of the infilling sediments of the Grotta Gigante cave is lower. However, as the synthetic models suggested, an internal gravity survey could be of interest for a better assessment of the infilling sediments' depth and for detecting other eventual karstic shafts or conduits.

To conclude, we point out that the Grotta Gigante cave is of great interest for gravimetric studies. The knowledge of the exact underground density distribution together with a clear gravity anomaly, well explained by our model, is very uncommon in other geologic contexts. The density 3D model and the gravity observed values constitute a unique data set, ideal for the testing of gravity forward and inverse algorithms.

ACKNOWLEDGMENTS

REFERENCES

Busà, G., 1975, Indagine morfologica per la verifica di una ipotesi sulla genesi della Grotta Gigante: Bollettino della Società Italiana di Topografia e Fotogrammetria, **2**, 1–16.

Caffau, E., F. Coren, and G. Giannini, 1997, Underground cosmic-ray measurement for morphological reconstruction of the "Grotta Gigante" natural cave: Nuclear Instruments and Methods in Physics Research A, **385**, 480–488, doi: 10.1016/S0168-9002(96)01041-8.

Carulli, G. B., and R. Onofri, 1969, I marmi del Carso: Del Bianco.

Cleveland, W. S., E. Grosse, and W. M. Shyu, 1992, Local regression models. Statistical models in S: Cole Advanced Books & Software.

Costa, G., L. Moratto, and P. Suhadolc, 2010, The Friuli Venezia Giulia accelerometric network — RAF: Bulletin of Earthquake Engineering, **8**, 1141–1157, doi: 10.1007/s10518-009-9157-y.

Cucchi, F., G. Casagrande, P. Manca, and L. Zini, 2001, Il Timavo ipogeo tra l'Abisso di Trebiciano e la Grotta Meravigliosa di Lazzaro Jerko: Le Grotte d'Italia, **2**, 39–48.

Cucchi, F., and E. Marinetti, 2000, Sosta 1.6 Grotta Gigante, in G. B. Carulli, ed., Guida alle escursioni. 80a riunione estiva della Societa Geologica Italiana: Università di Trieste, 213–216.

Cucchi, F., and C. Piano, 2013, Brevi note illustrative della carta geologica del Carso Classico Italiano: Regione Autonoma Friuli Venezia-Giulia.

Del Maschio, F., C. Giovani, M. Garavaglia, and L. Piccini, 2011, Anomalie di Radon in Grotta Gigante: Presented at Atti del convegno nazionale AIRP di radioprotezione, 488–506.

European Marine and Observation Data Network, 2006, Bathymetry, http://www.emodnet.eu/bathymetry, accessed 1 July 2014.

Fingolo, M., L. Facco, A. Ceccato, C. Breganze, P. Paganini, and M. Cezza, 2011, Tra realta virtuale e rilievi 3D ad alta risoluzione: Veneto Geologi, **75**, 21–25.

Kaufmann, G., 2014, Geophysical mapping of solution and collapse sinkholes: Journal of Applied Geophysics, **111**, 271–288, doi: 10.1016/j.jappgeo.2014.10.011.

Martinez-Moreno, F. J., J. Galindo-Zaldívar, A. Pedrera, T. Teixido, P. Ruano, J. A. Peña, L. González-Castillo, A. Ruiz-Constán, M. López-Chicano, and W. Martín-Rosales, 2014, Integrated geophysical methods for studying the karst system of Gruta de las Maravillas (Aracena, Southwest Spain): Journal of Applied Geophysics, **107**, 149–162, doi: 10.1016/j.jappgeo.2014.05.021.

Marussi, A., 1953, Rilevamento fotogrammetrico della Grotta Gigante presso Trieste: Alpi Giulie, **52**, 5–11.

Marussi, A., 1960, The University of Trieste station for the study of the tides of the vertical in the Grotta Gigante: Proceedings of 3rd International Symposium Earth Tides, 45–52.

Nagy, D., G. Papp, and J. Benedek, 2000, The gravitational potential and its derivatives for the prism: Journal of Geodesy, **74**, 552–560, doi: 10.1007/s001900000116.

Paganini, P., and A. Pavan, 2012, Rilievo laser-scanner della Grotta Gigante: Relazione Tecnica, Progressione. Supplemento semestrale ad "Atti e memorie", **58**, 129–132.

Regione Autonoma Friuli Venezia Giulia, 2006, Cartografia: ricerca alfanumerica, http://www.irdat.regione.fvg.it/CTRN, accessed 1 July 2014.

Regione Autonoma Friuli Venezia Giulia, 2010, Catasto Regionale delle Grotte del Friuli Venezia Giulia, http://www.catastogrotte.it/dettaglio_grotta.php?ID=2, accessed 1 July 2014.

Torge, W., 2001, Geodesy: De Gruyter.

Turner, D. A., I. J. Anderson, J. C. Mason, and M. G. Cox, 1999, An algorithm for fitting an ellipsoid to data: CiteseerXBeta, http://citeseerx.ist.psu.edu/viewdoc/summary?, accessed 11 November 2013.

Uieda, L., N. Ussami, and C. Braitenberg, 2010, Computation of the gravity gradient tensor due to topographic masses using tesseroids: Eos Transactions AGU, 91, Meeting of the Americas supplement, Abstract G22A–04.

USGS, 2006, Shuttle Radar Topography Mission, http://www.dds.cr.usgs.gov/srtm/version2_1/SRTM3/Eurasia/, accessed 1 July 2014.

Zanolla, C., F. Coren, F. Cucchi, F. Giorgetti, and M. Lovo, 1996, Elaborazione dei dati gravimetrici in corrispondenza della Grotta Gigante (Carso Classico, Trieste, Italia): Atti e Memorie della Commissione Grotte "E. Boegan", **33**, 17–24.